This is the accepted version of the paper.

This version of the publication may differ from the final published version.

Simulation of bubble expansion and collapse in the vicinity of a free surface

P. Koukouvinis [1,(a)], M. Gavaises [1], O. Supponen [2], M. Farhat [2]

[1]*City University London, Northampton Square, London EC1V 0HB, United Kingdom*

[2] *EPFL-LMH, Avenue de Cour 33 Bis, CH-1007 Lausanne*

Abstract. The present paper focuses on the numerical simulation of the interaction of laser-generated bubbles with a free surface, including comparison of the results with instances from high-speed videos of the experiment. The Volume Of Fluid (VOF) method was employed for tracking liquid and gas phases, while compressibility effects were introduced with appropriate equations of state for each phase. Initial conditions of the bubble pressure were estimated through the traditional Rayleigh Plesset equation. The simulated bubble expands in a non-spherically symmetric way, due to the interference of the free surface, obtaining an oval shape at the maximum size. During collapse a jet with mushroom cap is formed at the axis of symmetry, with the same direction as the gravity vector, which splits the initial bubble to an agglomeration of toroidal structures. Overall, the simulation results are in agreement with the experimental images, both quantitatively and qualitatively, while pressure waves are predicted both during the expansion and the collapse of the bubble. Minor discrepancies in the jet velocity and collapse rate are found and are attributed to the thermodynamic closure of the gas inside the bubble.

I. INTRODUCTION

The process of bubble growth and collapse is the core phenomenon in cavitating flows as it is linked to cavitation erosion. Indeed, it is well documented that the formation of jets in cavitating flows can contribute to cavitation erosion, due to the focused way of transferring energy from the bubble to the nearby walls [1-3]. Bubble growth and collapse in infinite liquid can be predicted using the Rayleigh Plesset equation [4]; this equation is a simplified form of the Navier Stokes equations under the assumptions of spherical symmetry, incompressible liquid and negligible gas inertia inside the bubble[1]. Over time, extensions of the original Rayleigh-Plesset version have been formulated, including e.g. compressibility effects, see the Plesset and Zwick variant [4] or model the presence of nearby bubbles, see the Kubota et al. modification [5]. Unfortunately, the spherical symmetry assumption of the Rayleigh Plesset equation means that it cannot predict any jetting phenomena or other types of asymmetries in the bubble development arising from the local flow field/boundary configuration/forcing terms.

In order to capture the asymmetric bubble interface due to the presence of the aforementioned conditions, it is necessary to solve the potential flow equations, commonly done using the Boundary Element Method (BEM), or the 2D axis-symmetric/3D Euler/Navier-Stokes equations. BEM methods are commonly used when high accuracy bubble dynamics is required or when simulating bubble clusters see e.g. [6, 7], however large deformations and topological changes of the bubble interface are somewhat problematic [8]. On the other hand, the Euler or Navier-Stokes equations have to be solved with an interface tracking or interface capturing technique to describe the bubble interface. Such

---

[(a)] Corresponding author, email: foivos.koukouvinis.1@city.ac.uk

46 works employ various techniques, from the Marker-and-Cell method of the pioneering work by
47 Plesset and Chapman [9], front tracking techniques by Hawker et al. [10], to Level-Set methodologies by
48 Lauer et al. [11]

49   In this work, the complicated interaction of a laser-generated bubble with the free surface of
50 initially stagnant water under earth gravity conditions is examined with CFD techniques. While
51 similar configurations have been simulated in the past with BEM (see for example, the work of
52 Robinson et al. [12]), the flow has not been investigated beyond the topological transformation of the
53 initial bubble to a torus. In the present work, the bubble interface is captured with the Volume Of
54 Fluid (VOF) method, capable of describing topological changes of the interface. Compressibility
55 effects in both gas and liquid phases are included, since they are essential to explain the formation of
56 secondary bubbly structures. The aim of this work is to try to replicate the experiments that have been
57 conducted so far at EPFL [13] with CFD, show the level of agreement and potential room of
58 improvement in the models. To be more precise the main features that this work aims to replicate are
59 the following:

60   - Macroscopic flow evolution (qualitative): the initially spherical bubble deforms due to the
61 presence of the free surface, obtaining an oval shape, then collapses. During the collapse a jet is
62 formed at the top of the bubble, with a direction towards the bottom of the container, piercing the
63 bubble and breaking into two toruses. The whole process is shown in Figure 1; it is, in general, axis-
64 symmetric, with the axis of symmetry being the vertical axis passing through the centre of the bubble.
65 Only at the very last stages of the bubble rebound significant asymmetry develops, due to turbulence
66 and accumulation of various disturbances (shown later, at Figure 10).
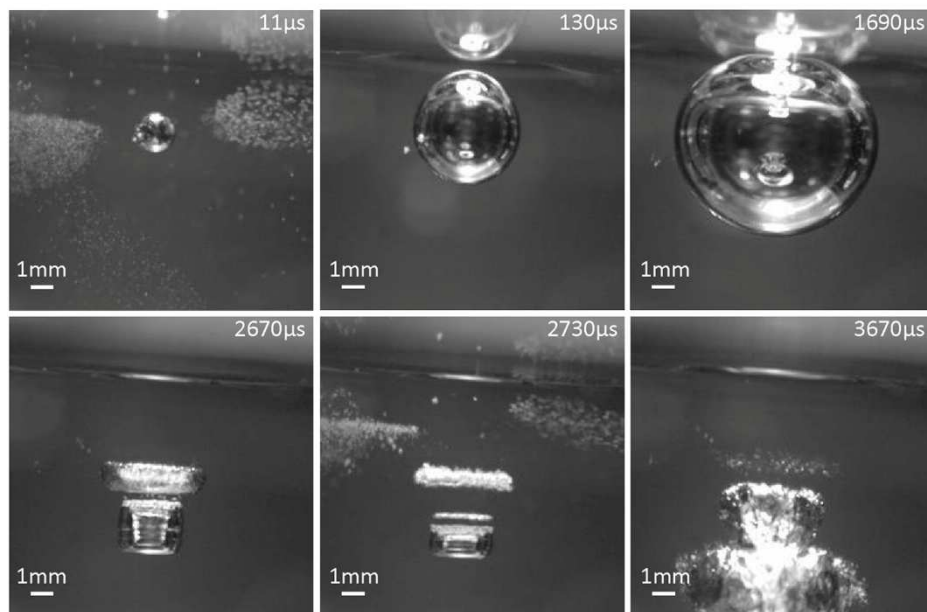

67
68   Figure 1. Evolution of the bubble shape near the free surface. The free surface position is visible through the reflection.
69   Gravity acts towards the bottom of the figures. The white bar at the bottom left corner corresponds to 1mm length.
70

71   - The time evolution of the bubble size (quantitative). Since the bubble very quickly deforms in a
72 shape that is not a perfect sphere, two characteristic dimensions of the bubbly structures will be used
73 for the comparisons to follow: (a) the maximum distance from the axis of symmetry of the bubble in
74 the horizontal direction, which will be referred to as radius (b) the bubble extent at the vertical
75 direction, which will be referred to as height. Also, once the bubble breaks into two toruses the one at
76 the upper part, near the free surface, will be referred to as *torus 1* and the other, which is closer to the
77 bottom of the container, will be referred to as *torus 2* - see also Figure 2.
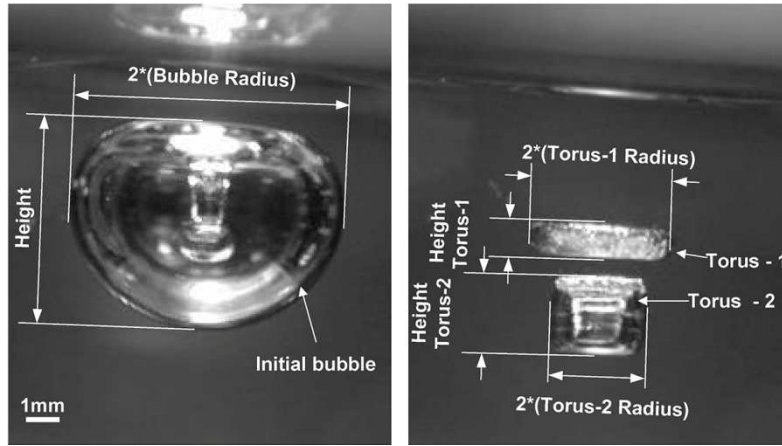
78

Figure 2. Bubble size naming convention that will be used hereafter and torus identification.

- Other geometric features of the bubble evolution (quantitative), that can be directly compared to the simulation, such as the jet diameter, maximum bubble radius etc.

The high-speed movies extracted from the experiment [13] have a resolution of 400x250pixels, with a scale of 17pixels corresponding to 1mm, so bubble dimensions can be derived.

II. EXPERIMENTAL SET-UP

A bubble collapsing near a free surface has experimentally been studied by Supponen et al. [13, 14] through high-speed imaging. In the experiment (details of the setup in [14]), a spherical cavitation bubble is created in water contained in a cubic ($18\times18\times18$ cm³) test chamber using a green, high-power laser pulse (wavelength 532 nm, duration 8 ns). The bubble is generated at distance of s=2.95 mm below the free surface. The bubble dynamics are visualised with a high-speed camera with speeds up to 50 000 frames per second. The experiment is conducted at room temperature and at low pressure (10.1 kPa=0.1 atm).

III. SIMULATION SET-UP

A. Geometry and computational mesh

The computational domain simulated is based on the dimensions of the test chamber that has been used for parabolic flights in the past (see previous section, or [15]). We have chosen to proceed with 2D axis-symmetric simulations for two reasons: (a) as will be shown later, the main process of the bubble growth and collapse are characterised by axial symmetry and only at the last stages of the experiment, after the rebound of bubbly structures, significant asymmetry develops (b) pursuing a full 3D simulation would be very computationally expensive. A 2D rectangular domain of 89.1 x 190.2mm was used, which corresponds to a cylinder of 178.2mm diameter. The influence of the boundaries is expected to be weak, since the maximum bubble radius examined is ~5.2mm.

The computational domain is positioned in such a way that the point (0, 0) corresponds to the axis of symmetry at the initial free surface level (see Figure 3). No-slip wall boundary conditions are placed at the side and the bottom of the container and fixed pressure at the open top of the container. In the experiments the container is connected to a vacuum pump that achieves the desired pressure level.
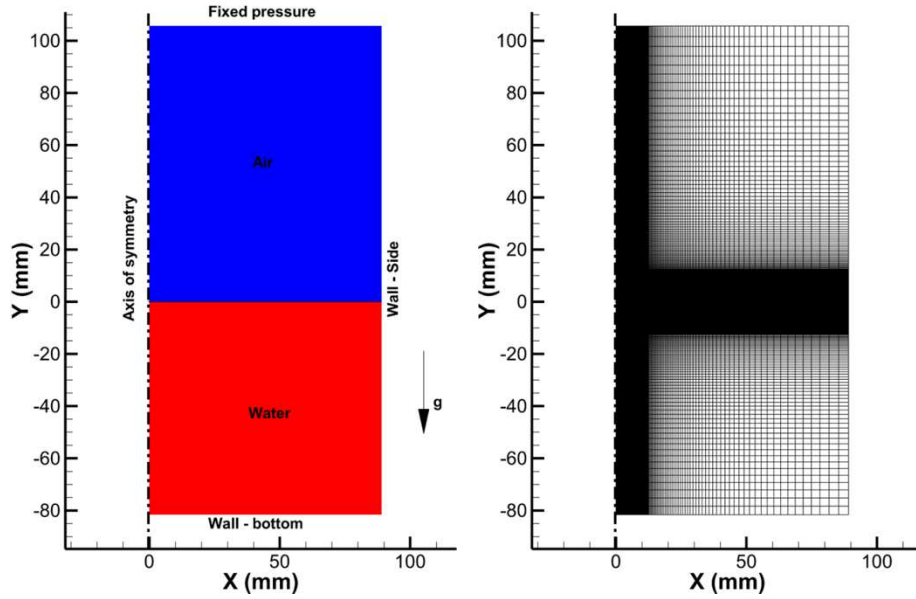
114
115 Figure 3. Configuration used for the simulation. Left: the 2D computational domain used. Right: the mapped computational
116 mesh with refinement in the area of interest.
117

118   The 2D rectangular domain was meshed with a mapped-type structured mesh [16], with local
119 refinement in the area of interest, which spans in the x-direction from 0 to 12mm and in y-direction
120 from -12 to 12mm. The aim of this refinement region is to capture with adequate resolution the bubble
121 growth and collapse, without needing an excessive amount of computational elements in the whole
122 container. The computational domain consists of 180000cells and in the area of interest the cell size is
123 50μm.
124   The container is initially filled with 84.5mm of water, as in the experiment. The ambient pressure
125 the experiment was conducted is p_{amb}~10320Pa. This pressure is imposed at the fixed pressure
126 boundary and is initially set at the air region of the computational domain. The hydrostatic component
127 of the air column is omitted since it is insignificant (at an estimated air density of 0.12kg/m^3, the
128 hydrostatic pressure of the air column is ~0.12Pa). On the other hand, the water part is initialized with
129 the hydrostatic pressure, since its contribution is not insignificant. Indeed, the hydrostatic pressure
130 difference from free surface to the bottom of the container is ~800Pa, or ~7% of the ambient pressure
131 level. Earth gravity (g=9.81m/s^2) is applied as an external forcing term at the -y direction.
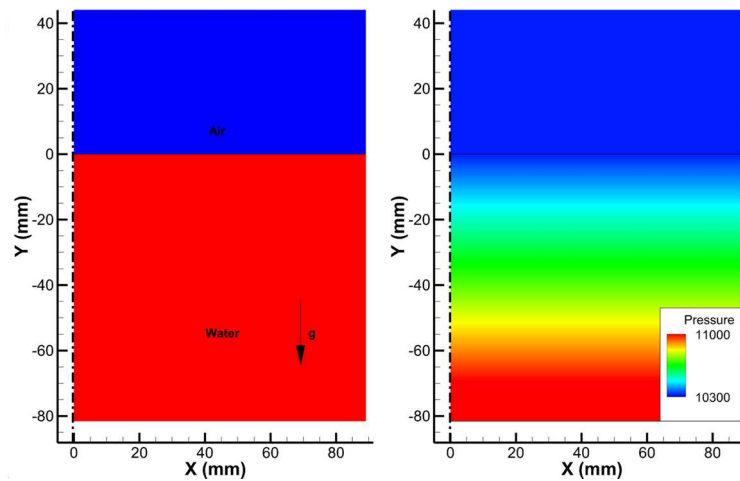
132

133
134 Figure 4. Initial phases and pressure distribution inside the container.

135

136   The laser-generated bubble is introduced as a high pressure gas bubble, as in the relevant work of
137   Ando et al.[17], located at the same location as in the experiments, i.e. at a distance s=2.95mm below the
138   free surface. This is done by patching an amount of gas in a circular shape with centre coordinates (0,
139   -2.95mm), initial radius R_0 and initial pressure p_0, see Figure 5. Initial radius R_0 should be as close as
140   possible to the initial bubble radius of the experiment. However this poses several challenges, since
141   the initial bubble is ~100 times smaller than the maximum bubble size [15], thus a very high grid
142   resolution would be required to capture it. Additionally, the state of fluid inside this bubble probably
143   departs from traditional fluid states, such as gas or liquid, due to the extreme initial conditions of the
144   bubble. On the other hand, if one desires to patch a larger bubble, then it would be necessary to
145   introduce the relevant velocity field generated by the bubble expansion. While this could be done in a
146   perfectly spherical bubble in a spherically symmetric environment, it is not possible such a shortcut to
147   be applied here, since there is a strong deviation from spherical symmetry due to the pressure gradient
148   and the free surface. It becomes apparent that a compromise has to be made. A smaller bubble would
149   be closer to reality, but it would require extreme resolution to capture, not to mention the questionable
150   nature of the fluid inside it. On the other hand, a larger bubble would be easier to simulate but it will
151   be difficult/impossible to initialize properly the consistent velocity field around it. For the given
152   configuration it was found that an initial bubble size of 0.1mm was enough to describe properly the
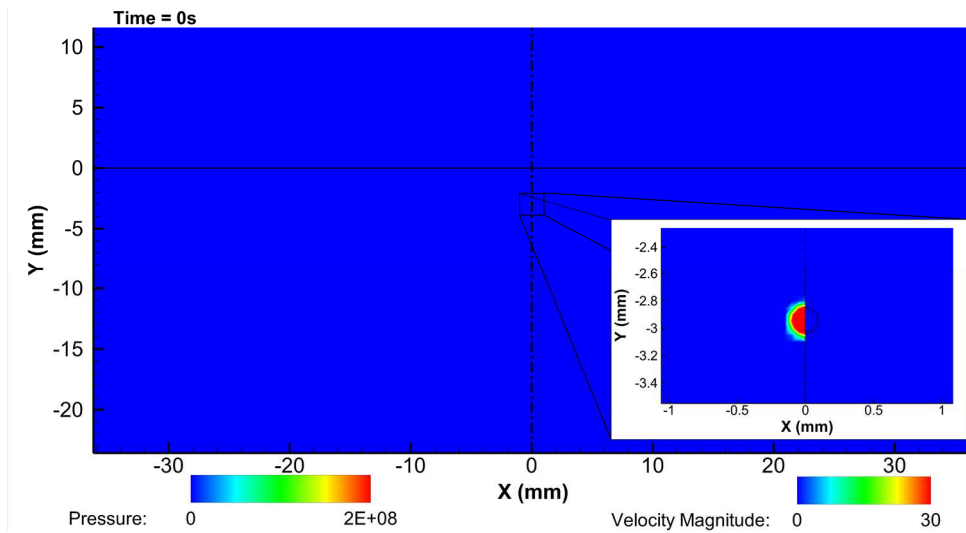153   bubble growth, giving results in accordance to the experiment.

154

155

Figure 5. Initial conditions for the bubble interaction with the free surface. The frame at the bottom right is a zoomed in view
at the initial bubble location.

158

159   The choice of the initial pressure and radius is also not trivial, since there is no simple
160   methodology correlating the temporal evolution of the actual bubble size, given the initial pressure,
161   due to the asymmetric expansion of the bubble. Still, a quick estimation can be made through the
162   Rayleigh-Plesset equation in the sense that initial pressures that predict a spherical bubble radius less
163   than the maximum found from the experiments can be safely discarded. The standard Rayleigh-
164   Plesset equation [1] was used, in the form:

$$\rho\left[R\ddot{R} + \frac{3}{2}\dot{R}^2 \right] = p_v - p_\infty + p_{g0}\left(\frac{R_0}{R} \right)^{3n} - \frac{2\sigma}{R} - 4\mu\frac{\dot{R}}{R} \tag{1}$$

166   where:
167   - ρ is the water liquid density, 998.2kg/m^3

168   - R is the bubble radius, $\dot{R} = dR/dt$ and $\ddot{R} = d^2R/dt^2$

169   - p_v is the vapour pressure.

170   - p_∞ is the pressure at the bubble level, including the hydrostatic pressure, i.e. $p_\infty = p_{amb} + \rho gs$, thus

171   p_∞ =10350Pa.

172   - p_{g0} is the initial bubble pressure, tuned to predict a similar maximum bubble radius as the
173   experiment.

174   - σ is surface tension, equal to 0.072N/m. It has to be highlighted that surface tension, even if
175   included, has a nearly unnoticeable effect. Collapse time is affected less than 0.3% and maximum
176   radius less than 0.15% with the inclusion of surface tension.

177   - μ is the dynamic viscosity of water, i.e. $1.01 \cdot 10^{-3}$Pa.s

178   - n is a polytropic exponent, depending on the thermodynamic process inside the bubble, e.g. for
179   adiabatic it is equal to the heat capacity ratio and for isothermal it is unity. In this study a value close
180   to unity has been used, since it matches better the experimental data.

181   In the present investigation, the vapour pressure is ignored. Whereas the vapour pressure is
182   definitely not insignificant, the fast expansion and collapse of the bubble poses some questions on
183   whether the mass transfer through the bubble interface is fast enough so that the vapour pressure
184   inside the bubble is always equal to saturation pressure.

185   Assuming an initial pressure p_{g0} of 1000bar for an initial bubble R_0=0.1mm, one obtains the
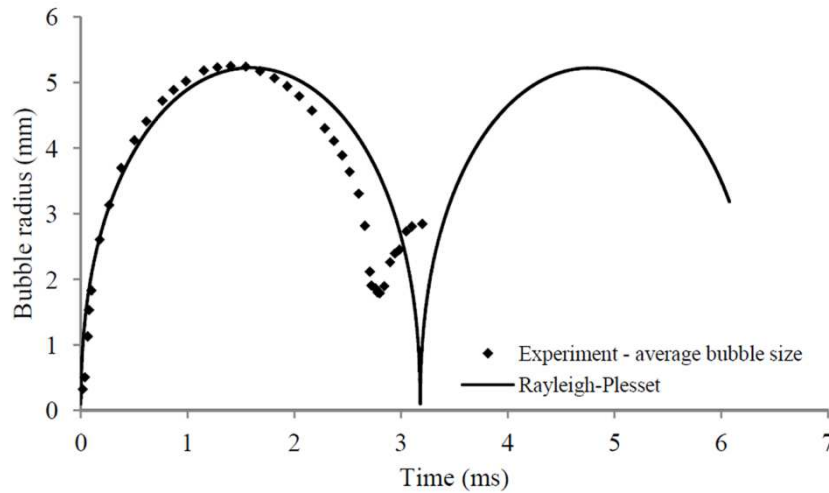186   following evolution of bubble size:

187
188 Figure 6. Time evolution of the experimental bubble size and comparison with the Rayleigh-Plesset solution for R_0=0.1mm
189 and p_{g0}=1000bar.

190   The deviation between the bubble development in the experiment and the solution of the Rayleigh-
191   Plesset equation should be expected, given the assumptions of spherical symmetry and infinite space
192   of the latter. In any case, considering the results in Figure 6, it becomes apparent that one needs at
193   least an initial pressure level of 1000bar in a bubble for an initial radius of 0.1mm, in order to be able
194   to reach a maximum radius of ~5mm. This greatly limits the number of trial-and-error runs that have
195   to be conducted to find the appropriate pressure level that gives the same maximum radius as in the
196   experiment.

197

198 **B.   Numerical model**

199

200   The numerical model that was used for the CFD simulations is based on the Volume Of Fluid
201   (VOF) method, since it is of interest to maintain a sharp interface between the two involved phases,

202 with topological changes of the interface. As mentioned, only water and gas are considered, whereas
203 vapour presence and mass transfer is ignored. The justification of this assumption is the fast process
204 of bubble growth and collapse that means there is little time available for effective mass transfer.

205   Continuity and momentum equations are solved, while thermal effects are ignored. The equations
206 solved, based on the viscous form of the Navier-Stokes equations, (for more information, the
207 interested reader is addressed to standard CFD textbooks, such as [18-21]), are as follows:

208   - Continuity equation:

209
$$\frac{\partial \rho}{\partial t} + \nabla \cdot (\rho \mathbf{u}) = 0 \tag{2}$$

210 where $\mathbf{u}$ denotes the velocity vector of the flow field.

211   - Momentum equation:

212
$$\frac{\partial \rho \mathbf{u}}{\partial t} + \nabla \cdot (\rho \mathbf{u} \otimes \mathbf{u}) = -\nabla p + \nabla \cdot \boldsymbol{\tau} + \rho \mathbf{g} + \mathbf{f} \tag{3}$$

213 where ρ is the density of the fluid, p is the pressure, $\mathbf{g}$ is the gravity vector, $\mathbf{f}$ are body forces and $\boldsymbol{\tau}$ is
214 the stress tensor, defined as follows:

215
$$\boldsymbol{\tau} = \mu\left[\nabla \mathbf{u} + (\nabla \mathbf{u})^{T}\right] + \lambda(\nabla \cdot \mathbf{u})\mathbf{I} \tag{4}$$

216   In eq. 4, $\mathbf{I}$ is the identity matrix and μ is the dynamic viscosity of the fluid; for the pure phases it is
217 set to 1mPa·s and 17.1μPa·s for water and air accordingly. Term λ denotes the bulk viscosity of the
218 fluid which acts only on passing waves; here it was set to -2/3μ, which is an assumption commonly
219 used, see [18, 19, 22]. Even if this value is mainly suggested for monoatomic gases [23], the simulation
220 results did not change significantly when using a value of 2.5mPa.s for water, as suggested by the
221 work of Holmes et al. [24]; to be precise, there was an indiscernible difference in the values of the
222 pressure field at the vicinity of the passing waves of ~0.14%. Since the effect of bulk viscosity is only
223 related to passing waves, it is unlikely to affect the general dynamics of the flow. Also, due to the
224 minor influence it was found to play, and due to the uncertainties in its values (for example Holmes et
225 al.[24] measured the aforementioned value for sound waves of minimum frequency of 15MHz for water
226 at 25°C, but it is known that there is a frequency dependence of λ [23]), it was decided to resort to the
227 more standard and commonly used value of -2/3μ, for which results will be presented hereafter. The
228 Reynolds number of the flow ranges around 10000 or less, for the majority of the simulation time, so
229 turbulence modelling has not been used.

230   Surface tension effects are included, employing the Continuum Surface Force Model which
231 represents surface tension as a volume force in cells where there is an interface, i.e. volume fraction
232 varies from zero to unity, see Brackbill[25]. The value for surface tension coefficient used is
233 σ=0.072N/m, as in the Rayleigh-Plesset equation in the previous section. In any case, surface tension
234 effects are considered minor, given an indicative Weber number of ~1400 for the jet inside the bubble.

235   - Volume fraction equation [26]:

236
$$\frac{\partial a\rho_{G}}{\partial t} + \nabla \cdot (a\rho_{G}\mathbf{u}) = 0 \tag{5}$$

237 where a represents the volume fraction and ρ_{G} the density of the gas phase. In the interface, where a
238 varies from zero to unity, volume fraction averaging is performed for determining the value of
239 viscosity and density.

240   Whereas in the actual experiment there is significant influence of heating effects, due to laser
241 interaction with the liquid, the resulting fluid state is not possible to describe with traditional equation
242 of states, such as ideal gas or other, since plasma generation and reactions take place. For this reason
243 some simplifications had to be made and the energy equation has been omitted, since it is redundant
244 in the thermodynamic closure chosen. Even with the omission of thermal effects, both phases are
245 assumed compressible, obeying the following equations of state:

246   - for the liquid, the Tait equation of state:

$$p = \frac{\rho_0 c_0^{\,2}}{n_l}\left(\left(\frac{\rho}{\rho_0}\right)^{n_l} - 1\right) + p_0 \tag{6}$$

248   where, ρ_0 is liquid density, equal to 998.2kg/m^3, c_0 the speed of sound, equal to 1450m/s, at the
249   reference state p_0=3490Pa. The exponent n_l is set to 7.15, according to relevant literature on weakly
250   compressible liquids, such as water [27]. Choice of the Tait equation of state is justified considering that
251   it matches closely the IAPWS liquid water data [28], comparing to simple linearized equations (as e.g. in
252   [29]), especially at extreme pressures, where the deviation in predicted densities may exceed 10%.
253   - for the gas, a polytropic equation of state is used:

$$p = k\rho^n \tag{7}$$

255   Constant k is case dependent; here it is set assuming a gas density of ~0.12kg/m^3 (calculated from
256   ideal gas for a temperature of 25°C) at the ambient pressure of 10320Pa. The exponent n is set close to
257   unity, as in the Rayleigh-Plesset equation. The reason for resorting to this equation of state is twofold;
258   first of all it is practically the same equation of state in the Rayleigh-Plesset equation. Secondly, it is a
259   simple equation that can describe the compression and expansion of the bubble with the omission of
260   thermal effects. For both equations of state, speed of sound c is defined as follows [30]:

$$c = \sqrt{\left(\frac{dp}{d\rho}\right)} \tag{8}$$

262   Equations (2) and (3) are solved with a pressure-based algorithm, i.e. a pressure correction
263   equation is solved. Then the pressure correction is linked to a velocity correction and to a density
264   correction through the speed of sound (eq. 8, see also [18, 31]), to satisfy mass balance of fluxes in each
265   cell. In order minimise the effect of numerical diffusion, which could affect the development of the
266   bubble during the whole process of growth and collapse, second order upwind schemes have been
267   used for the discretization of density and momentum, while the VOF phase field has been discretized
268   using a compressive differencing scheme [32] to maintain a sharp interface. Briefly stated here, the
269   particular scheme is based on high resolution differencing scheme and the Normalised Variable
270   Diagram to achieve boundedness; the interested reader is addressed to O. Ubbink PhD thesis [33], Ch. 4,
271   for more information. Time stepping is done with an adaptive method, to achieve a Courant-
272   Friedrichs-Lewy (CFL) condition [26] for the free surface propagation of 0.2. This is necessary, to limit
273   as much as possible the interface diffusion and maintain solution accuracy at near the free surface [34].
274   The solver used is implicit pressure based and this removes any restrictions on the acoustic courant
275   number, which is ~10 (on average) considering the minimum cell size and the maximum wave
276   velocity.

277

278 **IV. RESULTS**

279

280   The first step in the solution process is to determine the initial pressure p_{g0} inside the bubble for the
281   chosen radius R_0=0.1mm. As mentioned before, the solution of the Rayleigh-Plesset equation helps in
282   narrowing the possible pressure range, since a pressure level of at least 1000bar is required inside the
283   bubble. Starting from an initial pressure of e.g. 1500bar, a maximum bubble radius is predicted by the
284   Rayleigh Plesset equation. For the same conditions, the maximum bubble radius predicted by the
285   simulations was smaller; this is expected due to the asymmetric bubble expansion. The ratio between
286   the Navier Stokes and Rayleigh Plesset calculated radius was used to determine a correction factor.
287   Applying this correction factor to the Rayleigh Plesset equation enabled the calculation of a more
288   accurate prediction of the initial pressure that gives a maximum bubble radius of ~5.2mm. Potentially
289   the aforementioned process should be repeated several times, until the desired maximum radius is

290 achieved. However, in practice, only one iteration was needed to determine the initial pressure that
291 gives a maximum bubble radius of ~5.2mm, which is 2180bar.

292   In the following figures, selected instances of the developed flow field are shown. Each image is
293 separated by the axis of symmetry (dashed-dotted line) in two parts. The left part shows the pressure
294 field and the right part the velocity field. The thick black line indicates the liquid/gas interface. White
295 regions in the pressure field indicate tension and can be correlated to secondary bubble formation
296 found in the experiments. Note that the pressure/velocity scales are not the same, since there is a
297 strong variation over time. Whenever possible, images from high speed movies of the experiment are
298 provided; it must be highlighted that camera angle and lighting were chosen as to depict in the best
299 possible way the bubble shape evolution and not the shape of the free surface, which cannot be
300 derived from the present images. Indicative instances of the free surface shape can be found in a
301 recent work of Supponen et al.[14]. Alternatively, a video showing both the bubble and part of the free
302 surface can be found in the Gallery of Fluid Motion by the same authors [35].

303   A very important observation is the fact that during the expansion of the bubble, a shock wave is
304 emitted. When this shock wave interacts with the free surface, part of it is transmitted in air as a weak
305 shock wave, whereas a significant part is reflected back in the liquid as a Prandtl-Meyer rarefaction
306 wave causing tension and resulting to the excitation of bubbles to expand. This effect is well known in
307 the literature, in interactions of shock waves and free surfaces, see e.g. [17, 36-38]. The whole process of
308 shock wave interaction with the free surface is visible in Figure 7:

309   - At 2.8μs (Figure 7a) the shock wave expands in all directions, but reflects at the free surface,
310 forming a rarefaction wave and causing locally tension in the liquid between the bubble and the free
311 surface.

312   - At 5.3μs (Figure 7b) the tension wave moves and is located at the sides of the bubble, whereas
313 the shock wave further propagates.

314 - At 8.4μs (Figure 7c) the shock wave continues to expand closely followed by the tension wave. At a
315 similar time instant in the experiment (Figure 7d), secondary bubbles emerge at the sides and under
316 the bubble. During these early stages of bubble expansion the bubble shape remains close to spherical.

317   In all the aforementioned figures negative absolute pressures are shown in areas of tension. Such
318 pressures are naturally predicted by the Tait equation of state, since it represents the behaviour of a
319 weakly compressible elastic medium, such as liquid water. In reality, however, such magnitudes of
320 negative pressures may not appear, since secondary bubble generation, as shown in Figure 7d, will
321 relieve tension.

322   At later bubble growth stages, the bubble shape deviates from spherical and assumes an oval
323 shape, see Figure 8a or Figure 8c. This is a direct consequense of the lower inertia of the fluid towards
324 the free surface, causing a biased expansion towards the upwards direction. However, as the gas
325 inside the bubble expands pressure inside the bubble drops, eventually decelerating the expansion and
326 causing the collapse of the bubble. The maximum bubble radius predicted with CFD is ~5.3mm, close
327 to the one found from the experiment, which is 5.25mm, ensuring that the initial pressure estimation is
328 accurate enough, at least for the present study. During the collapse, a downwards moving jet is formed
329 (Figure 8e). The jet is predicted to have a radius of ~0.5mm, which is in agreement with the
330 experiment. However, contrary to the experiment the predicted jet velocity is somewhat higher: the
331 CFD results indicate a velocity of ~14m/s, whereas the jet velocity in the experiment is ~9m/s. This
332 discrepancy, which is also found in the slightly faster collapse of the CFD simulation in respect to the
333 experiment, was found to be unrelated to the mesh resolution (finer mesh yielded differences less than
334 1% in e.g. jet velocity). Additionally the bubble mass is conserved with a maximum error of 0.15%,
335 thus the mismatch is mainly attributed to the thermodynamic model of the gas inside the bubble,
336 rather than numerical inaccuracies. Still for the level of complexity involved the results can be

considered acceptable. Another potential source of the discrepancy is experimental error due to optical distortion of the jet from the bubble wall.
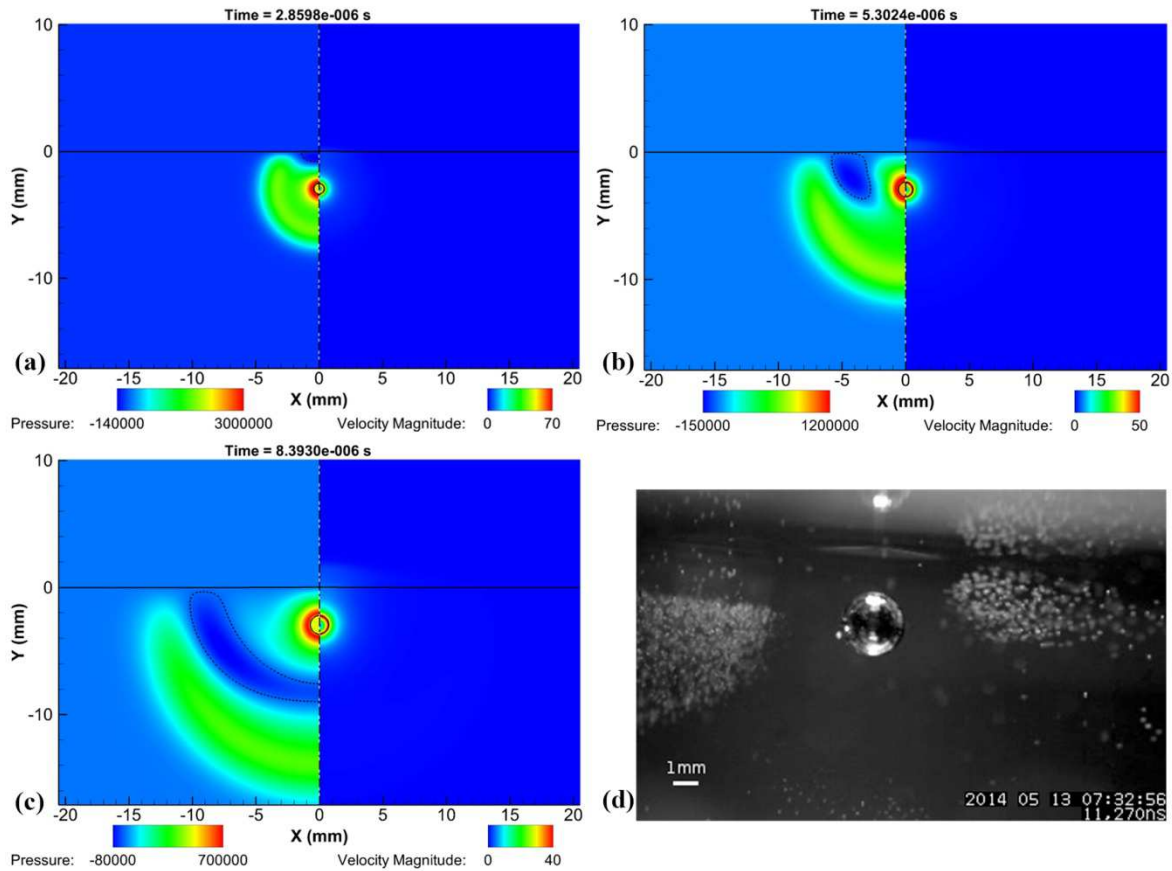

Figure 7. Initial stages of bubble expansion. Note that the dashed line delimits the liquid under tension; this effect can be correlated to the formation of smaller bubbles near the main bubble.

Another interesting effect that is found at the jet is the mushroom cap (see Figure 8e, f); this effect is the manifestation of well known interfacial instabilities, like the Rayleigh-Taylor or the Richtmyer–Meshkov instabilities [39]. The radius of the jet cap is predicted to be ~1mm, in accordance with measurements from the experiment, see [14].

After the jet impacts the bottom of the bubble, it deforms it in such a way that a gaseous pocket is formed, see Figure 9a, b. Later on the gaseous pocket detaches from the initial bubble. The initial bubble has a toroidal structure from now on (referenced as torus-1), since it has been pierced by the jet. The detached pocket has also a toroidal structure (Figure 9c, denoted as torus-2), as shown from the simulation. Evidence of the toroidal structure of the gas pocket is found from the photos of the experiment as well (Figure 9d), since the light reflections inside the gas bubble indicate an internal structure in the form of a vertical liquid core. Both toruses further collapse and expand again; torus - 1 remains relatively intact, whereas torus - 2 splits further (Figure 9e, f). At later stages, torus-2 collapses and then further splits, see Figure 10a, b. All toroidal bubbly structures start to expand and form an agglomeration, see Figure 10c, d.

The suspected mechanism of the splitting of torus-2 is shear layer instability, which potentially could be related to the Kelvin Helmholtz instability, since there is shear across a fluid interface. As shown in Figure 11 there is significant vorticity in the toroidal structures located at the lateral surface of the downwards moving liquid jet.
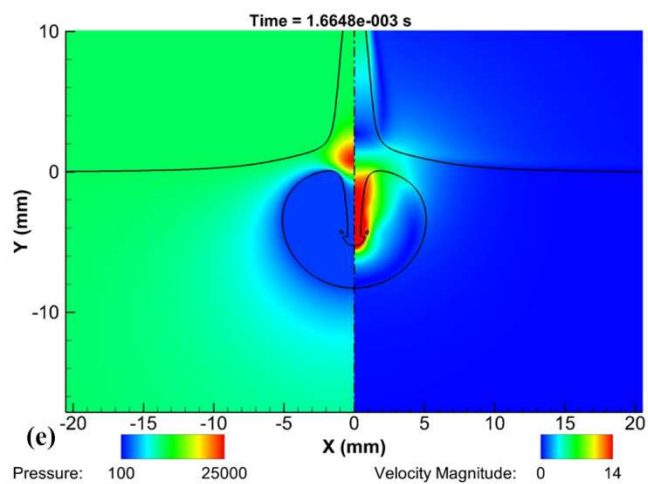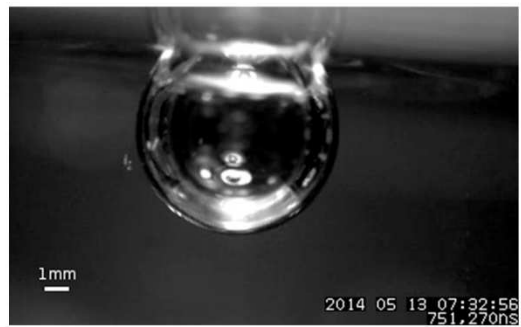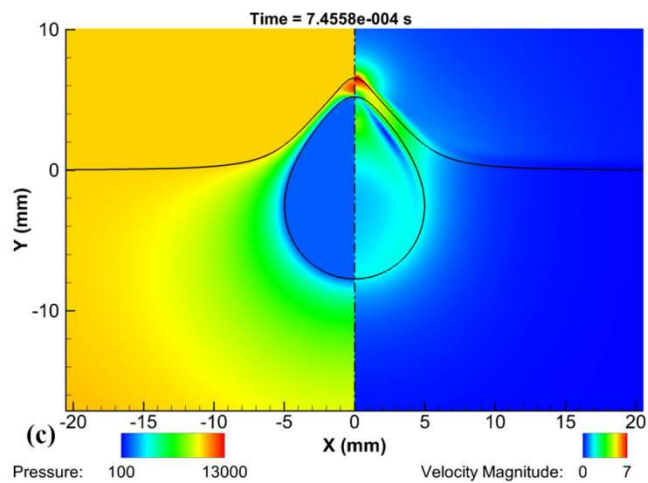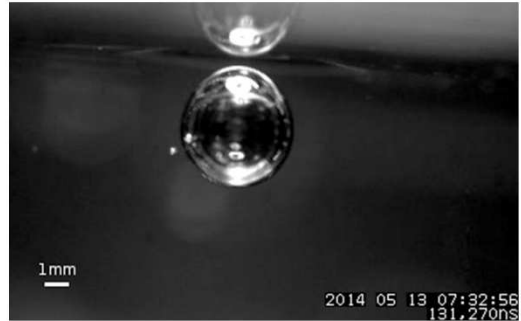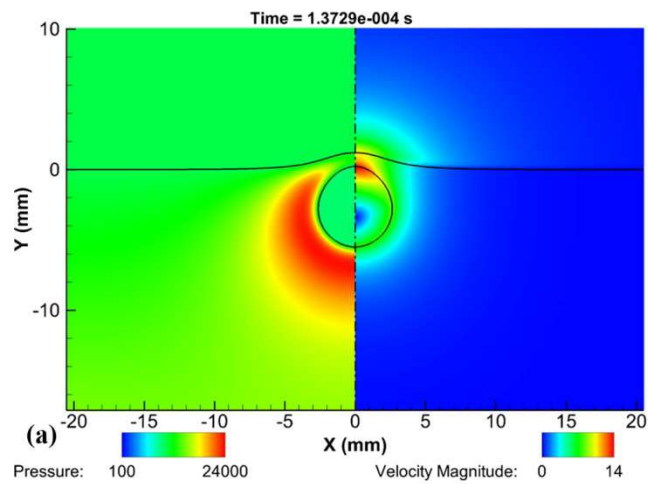
Figure 8. Later stages of bubble deformation. Note the deviation from spherical shape to an oval-like shape, while later a downwards moving jet is formed.
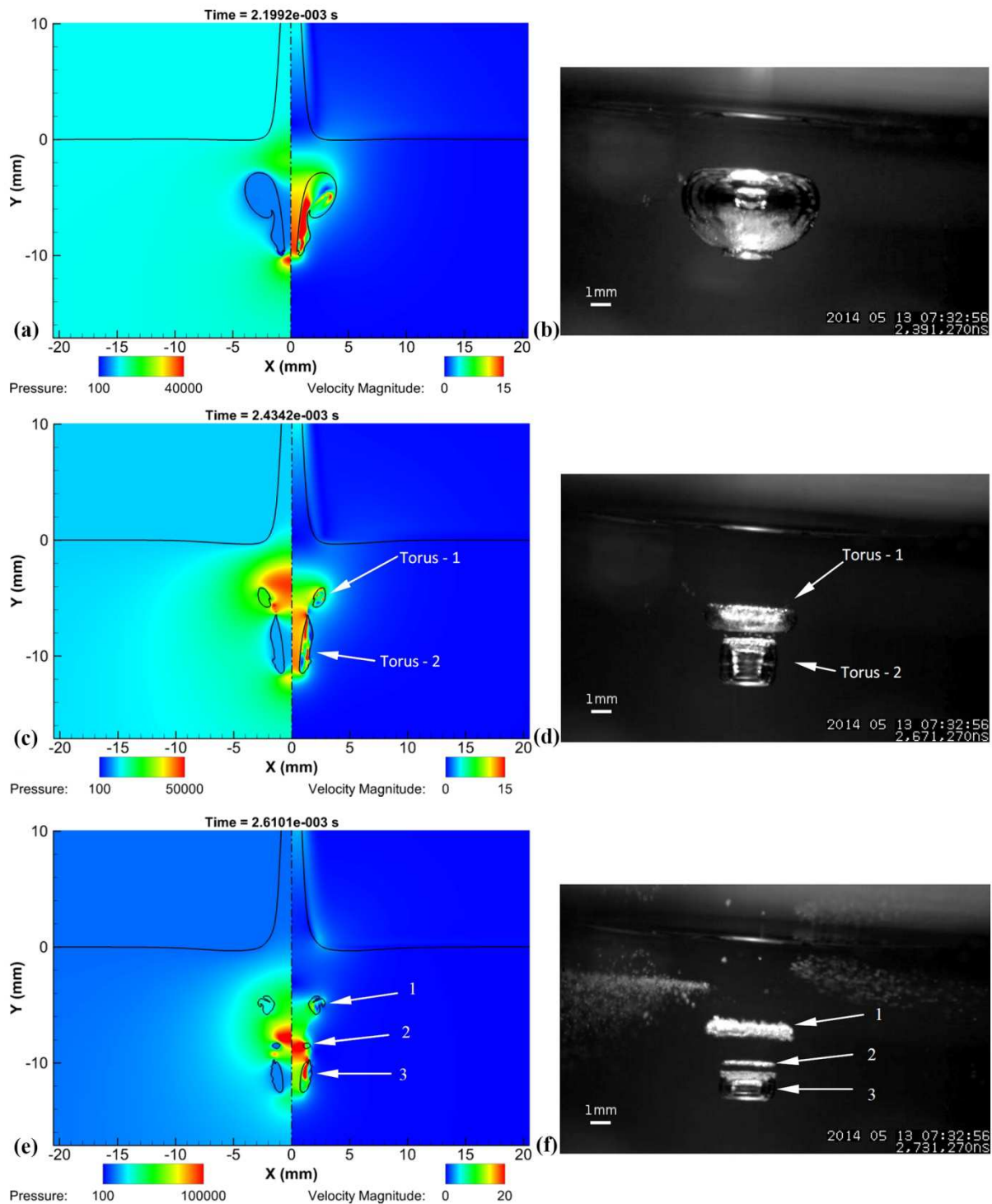
366
367
368
369
370
371
372
373

374
375

Figure 9. Development of the toruses after the jet impact. Further splitting of torus-2 is visible at 2.6-2.7ms. Similar structures are identified with similar numbering between the CFD and experiment.

376
377
378
379
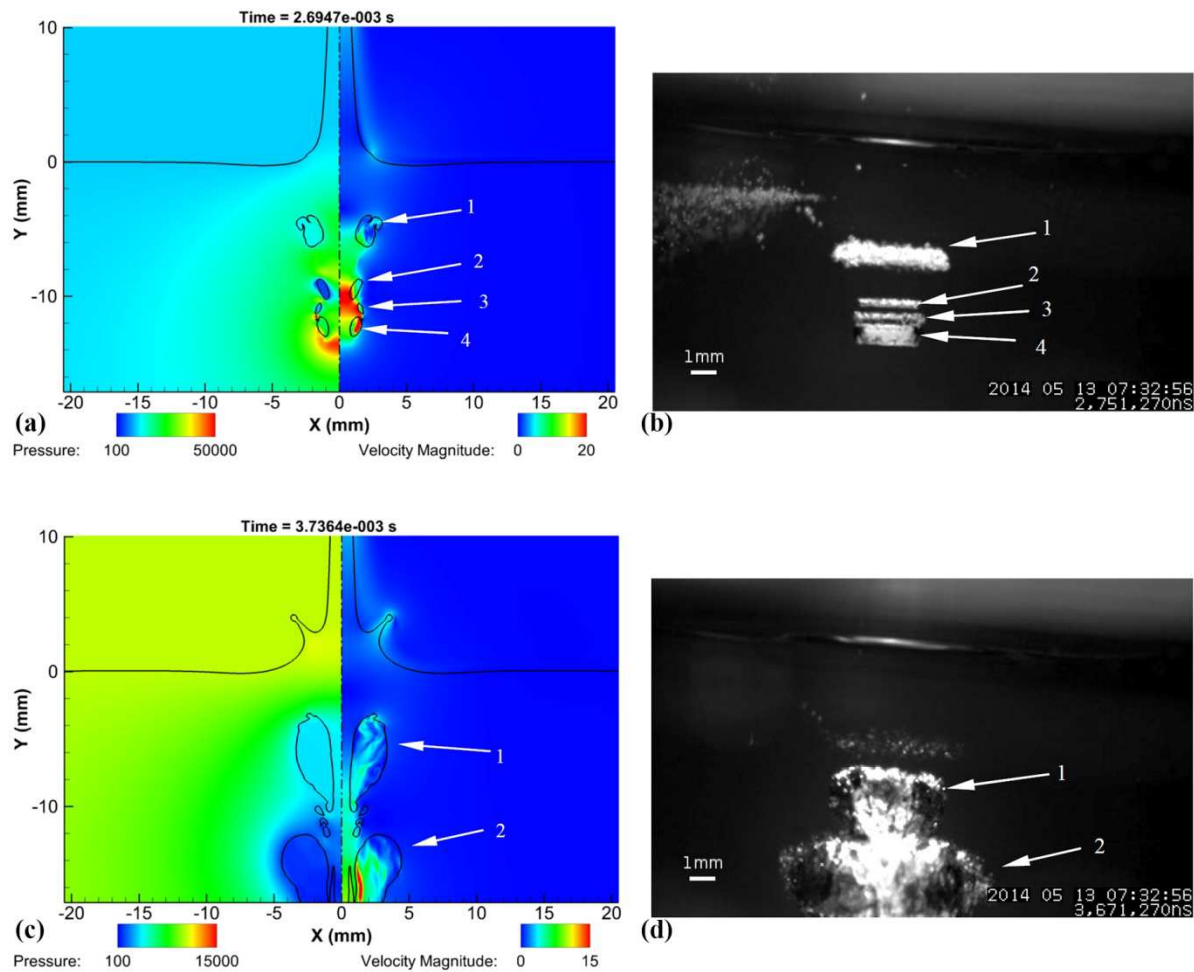380
381
382
383
384
385

386

Figure 10. Late development of the toruses after the jet impact; further splitting of torus 2 is visible, as well as the expansion of the toruses. Similar structures are identified with similar numbering between the CFD and experiment. The formation of a corona at the free surface is visible, see also [13, 14]

In Figure 12, the laplacian of the density field is shown, for selected instances of the simulation, to depict a numerical shadowgraph image [40] from the simulation:

- At the instance of 35.4μs a strong shock wave is visible expanding in an arc-like shape in the water volume. Also a much weaker shock wave can be observed in the air volume, just above the epicentre of the bubble expansion. Both of these shock waves are formed due to the initial bubble expansion.

- At 137μs there is an interference pattern inside the liquid volume, due to reflection of pressure waves at the walls. The much weaker shock wave travelling in air, above the liquid, is still expanding and visible.

- Later on, at 1.865ms a shock wave is formed due to the impact of the jet on the bubble wall.

- At 2.53ms several shock waves are emitted, due to the collapse of torus-1.

In Figure 13(multimedia view) an animation of the bubble development is shown, as predicted by the simulation, for the better understanding of the bubble shape evolution and the relevant deformation of the free surface.
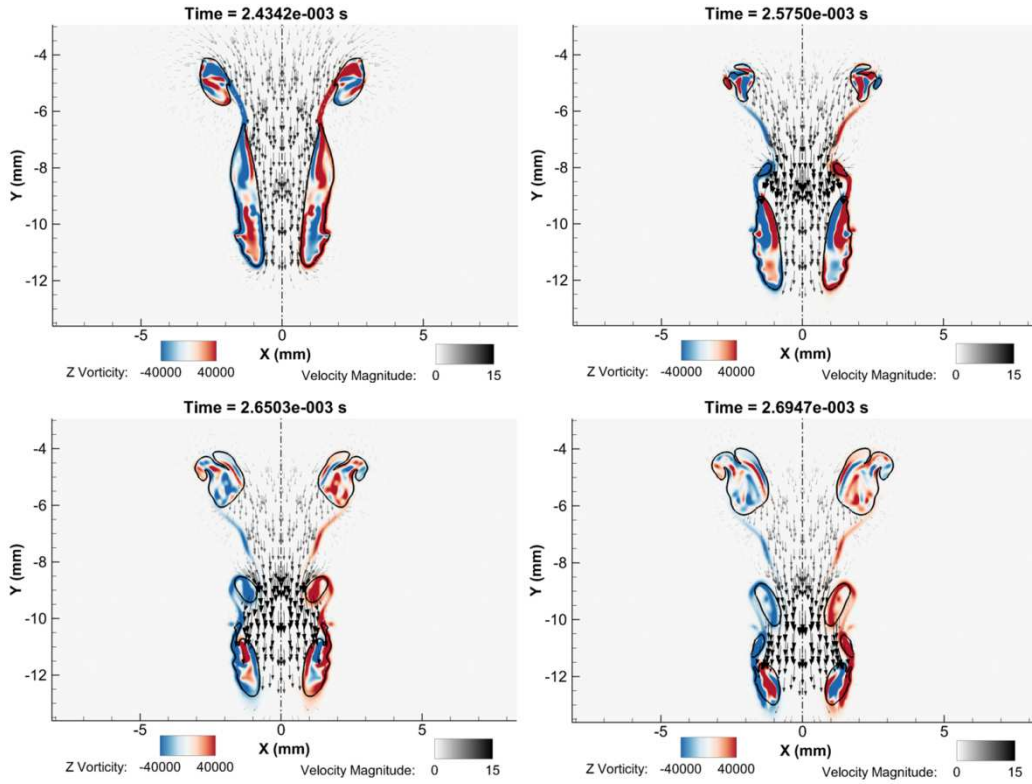
407
408   Figure 11. Vorticity contours in the vicinity of the gas toruses during break-up. Velocity vectors are included to show the
409   liquid jet. Red colour indicates counter-clockwise vortices, whereas blue colour clockwise vortices. The liquid/gas interface
410   is shown as a black line. Vectors are plotted on cell nodes and only one every 25 vectors is shown for clarity.
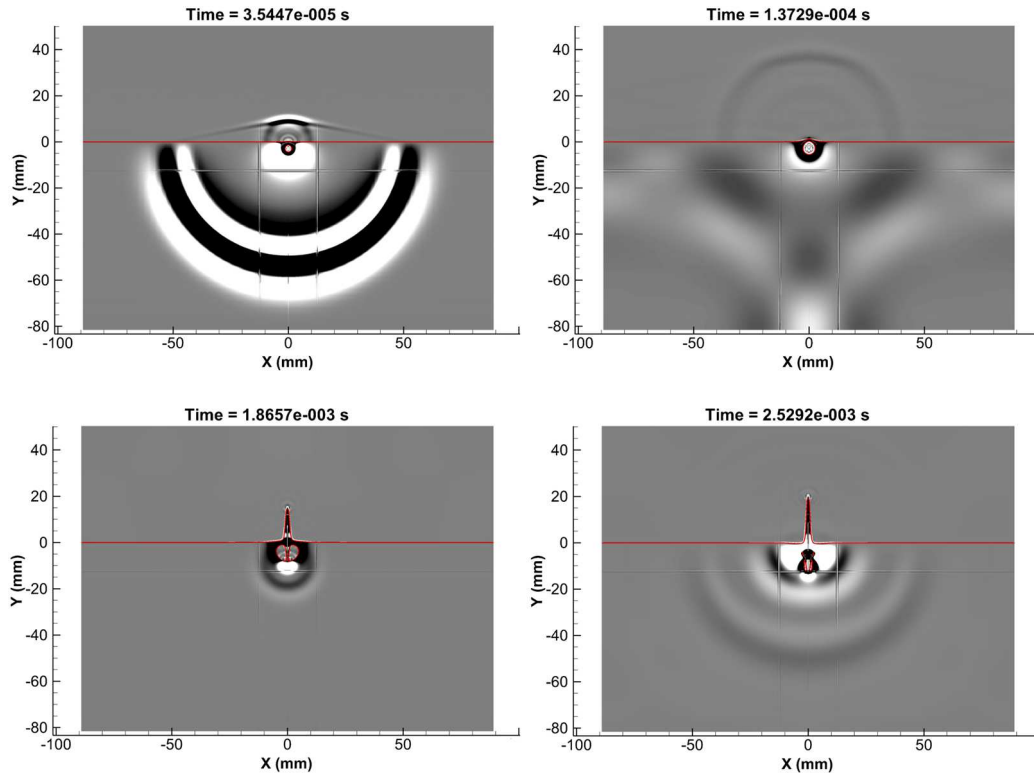
411

412
413   Figure 12. Numerical shadowgraph images (laplacian of the density field), showing the propagation of pressure waves, due
414   to the expansion and collapse of the bubbly structures. The gas/liquid interface is shown as a continuous red line.
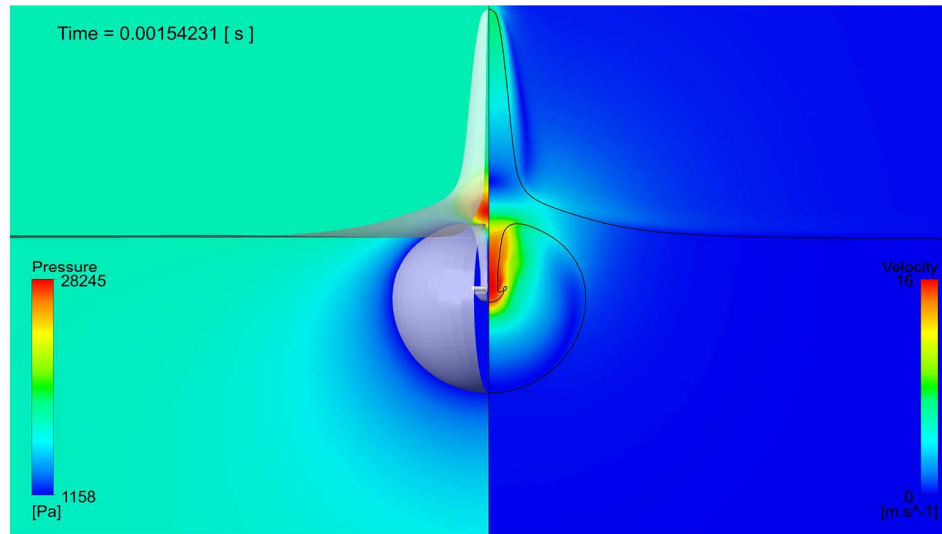
415

Figure 13. Animation of the simulation results of the bubble/free surface interaction. The video is split in the middle with a vertical continuous line. The left part shows the pressure field, while the grey isosurface is a 3D reconstruction of the liquid/gas interface. The right part shows the velocity magnitude, while the continuous black line shows the interface. Units are in SI (i.e. pressure in Pascal and velocity in m/s). (Multimedia view)

V. DISCUSSION

In Figure 14 the time evolution of the bubble radius and bubble height is presented, as found from the experiment [14] and the CFD simulation. It is visible that the predicted collapse from CFD is somewhat faster. Collapse of torus - 1 is found at 2.53ms, whereas in the experiment it occurs at ~2.7ms, i.e. there is an error of ~6%. Still, the overall agreement of the bubble size evolution between CFD and experiment is good, given the complexity of the problem and the simplicity of the thermodynamic model of the gas involved, which is believed to be the main source of inaccuracy. Unfortunately, due to the very complicated nature of the process inside the gas bubble, especially during its generation, it was not possible at the current stage to employ a better model.

In any case, given the results of the study the following conclusions may be reached:

- In general, the whole process of bubble expansion and collapse is captured. Fine details such as the formation of the tension waves, bubble shape and bubble breaking, jet size with mushroom-shaped tip and finally the corona formation are captured.

- Even if surface tension has been included, its effect is nearly unnoticeable. This is justified by the fact that the growth/collapse process at these bubble sizes is mainly inertial dominated: for example, as mentioned above, bubble collapse time is affected less than 0.3% as found from the Rayleigh-Plesset equation. The only exception of this is the formation of the corona, where local Weber number is ~50.

- The thermodynamic model of the gas employed is simplistic, but can provide a simple methodology for including the bubble gas effects without needing to resort to exotic equations of state or other advanced techniques, with good accuracy in respect to reality.
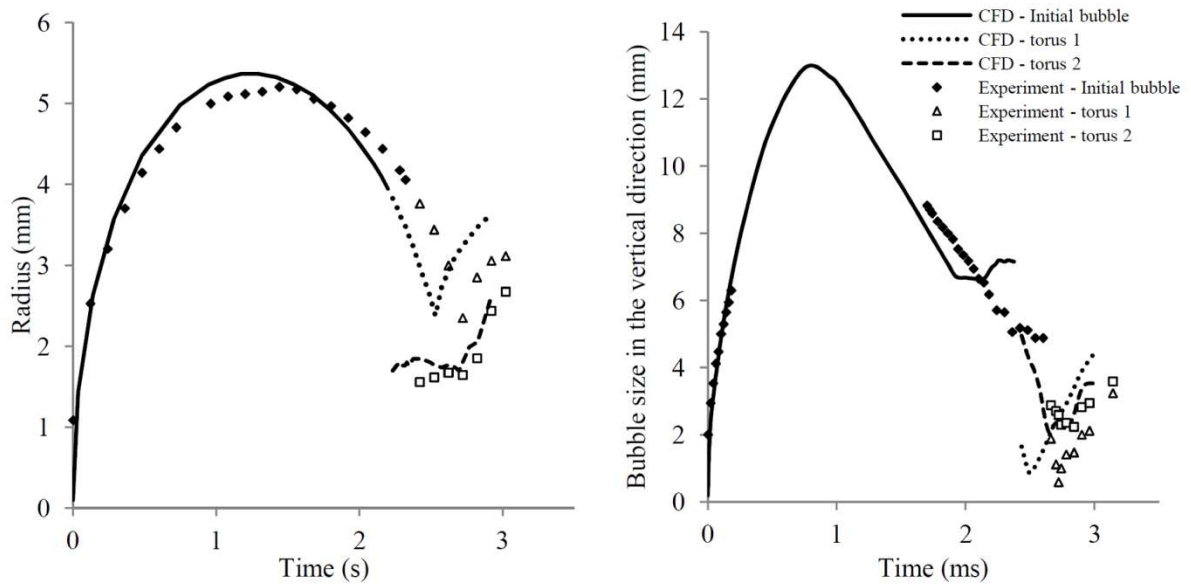
445

Figure 14. Time evolution of the bubble size for the initial bubble and the two toruses formed after the jet impact. Comparison of the CFD and experimental results [14].

In case a more accurate representation of the bubble gas is required, there are two main directions to be pursued:

1. One is to include the mass transfer from liquid water to vapour. In the Rayleigh-Plesset equation the mass transfer rate is assumed to be infinite, since vapour pressure inside the bubble is always equal to saturation pressure. In reality the mass transfer is finite, however the formulations used in the literature are based on the Hertz-Knudsen evaporation/condensation formula [41], which depends on molecular characteristics, such as the accommodation coefficient [4], see e.g. Lauer et al. [11] or Fuster et al. [42].

2. Another improvement is to include the thermal effects during bubble expansion and collapse. This will require to simulate the early stages of expansion at rather extreme conditions, since initial conditions for the temperature/internal energy will be needed. For example, in the present study the maximum bubble volume is ~600mm^3 and this corresponds to an energy of ~6.7mJ. Given though that some energy is dissipated to the rest of the liquid due to heating losses, it is reasonable to assume that the initial bubble seed is heated by ~12mJ of laser energy. Under the assumption that the initial bubble of R_0=0.1mm is almost instantaneously heated by this energy, thus the density change is almost insignificant, then the enthalpy rise is equal to ~3000kJ/kg. Unfortunately existing water/vapour libraries are rather inaccurate or not applicable at such conditions:

- The IAPWS-IF97 formulation which is probably the most accurate for water/steam [28], is not applicable for pressures beyond 1000bar and for highly superheat steam beyond 500bar.

- NIST databases [43], while could be used at such conditions, are of questionable accuracy; for the conditions mentioned above, i.e. density ~998.2kg/m^3 and enthalpy ~3000kj/kg the predicted fluid pressure is 11000bar and temperature 850K; in the authors' opinion the temperature look rather low (there are research studies predicting temperatures of the order of 10000K, see [44]), whereas pressure seems very high. Besides, the NIST database is a fitting of a Helmholtz energy or Benedict-Webb-Rubin equation of state to experimental data, thus accuracy at adverse conditions is not guaranteed. Needless to say that for 11000bar and 850K the ideal gas equation predicts a density of 2801.7kg/m^3.

While all the above are a rather crude estimate of the conditions at the beginning of the bubble expansion, it becomes apparent that there is an important problem of a consistent thermodynamic

478 closure at the conditions involved. More research is required on the subject, that probably departs
479 from traditional fluid dynamics, computational or experimental, since the conditions may involve
480 other effects as dissociation, reactions and plasma.
481
482 **VI. CONCLUSION**
483
484   In this work, a description of the interaction of a laser-generated bubble with free surface is
485 provided, comparing the results of experiments and CFD simulations based on the VOF methodology.
486 Simulations were successful in the prediction of bubble expansion and collapse, both qualitatively and
487 quantitatively, whereas pressure wave propagation effects were identified. Fine details of the
488 liquid/gas interface were observed, such as the mushroom cap at the tip of the jet, or the splitting of
489 the torus-2 in an agglomeration of toroidal structures. While some deviations from the experimental
490 results exist, the overall qualitative and quantitative agreement is rather good, proving that CFD can
491 be an invaluable tool for shedding light to complicated bubble dynamics phenomena, in a non-
492 intrusive way. Potential improvements of the current study involve mainly the thermodynamics of the
493 gas inside the bubble.
494
495 **ACKNOWLEDGMENTS**
496

504
505 **Nomenclature**
506

s	Bubble generation depth (m)
p_{amb}	Ambient pressure (Pa)
ρ	Density (kg/m^3)
R	Bubble radius (m)
R_0	Initial bubble radius (m)
$\dot{R}$	Bubble interface velocity (m/s)
$\ddot{R}$	Bubble interface acceleration (m/s^2)
p_v	Vapour pressure (Pa)
p_∞	Far-field pressure (Pa)
p_{g0}	Initial gas pressure (Pa)
σ	Surface tension (N/m)
μ	Dynamic viscosity (Pa·s)
u	Velocity vector field (m/s)
τ	Stress tensor (Pa)
g	Acceleration of gravity (m/s^2)
f	Body/volume forces vector (N/m^3)
λ	Bulk viscosity coefficient (Pa.s)
a	Gas volume fraction
n	Polytropic exponent (for gas) (-)
n_l	Tait equation exponent (for liquid) (-)
ρ_0	Reference density (kg/m^3)

c_0	Reference speed of sound (m/s)
p_0	Reference pressure (Pa)
k	Constant of polytropic gas process $\left(\dfrac{Pa}{\left(kg/m^3 \right)^n} \right)$

References

1. J.-P. Franc and J.-M. Michel, Fundamentals of Cavitation, (2005), Kluwer Academic Publishers.

2. M. Tinguely. The effect of pressure gradient on the collapse of cavitation bubbles in normal and reduced gravity, in *Faculté des sciences et techniques de l'ingénieur, Laboratoire de machines hydrauliques* (2013), Ecole Polytechnique Federale de Lausanne, Switzerland. p. 120.

3. G. L. Chahine, J.-P. Franc, and A. Karimi, Cavitation and Cavitation Erosion, in *Advanced Experimental and Numerical Techniques for Cavitation Erosion Prediction*, Kim K-H, et al., Editors. 2014, Springer Netherlands. p. 3-20.

4. C. E. Brennen, Cavitation and Bubble Dynamics, (1995), Oxford University Press.

5. A. Kubota, H. Kato, and H. Yamaguchi, A New Modelling of Cavitating Flows - a Numerical Study of Unsteady Cavitation on a Hydrofoil Section, *Journal of Fluid Mechanics* **240**, (1992), p. 59-96 DOI: 10.1017/S002211209200003X.

6. N. Mendez and R. Gonzalez-Cinca, Numerical study of bubble dynamics with the Boundary Element Method, *IOP Journal of Physics: Conference Series, International Symposium on Physical Sciences in Space* **327**, (2011), p. 9 DOI: 10.1088/1742-6596/327/1/012028.

7. G. L. Chahine, Modeling of Cavitation Dynamics and Interaction with Material, in *Advanced Experimental and Numerical Techniques for Cavitation Erosion Prediction*, Kim K-H, et al., Editors. 2014, Springer Netherlands. p. 123-161.

8. S. Sauter and C. Schwab, Boundary Element Methods, 1st ed, (2011), Springer-Verlag Berlin Heidelberg.

9. M. S. Plesset and R. B. Chapman, Collapse of an initially spherical vapor cavity in the neighborhood of a solid boundary, *Journal of Fluid Mechanics* **47**, (1971), p. 283-290 DOI: 10.1017/S0022112071001058.

10. N. A. Hawker and Y. Ventikos, Interaction of a strong shockwave with a gas bubble in a liquid medium: a numerical study, *Journal of Fluid Mechanics* **701**, (2012), p. 55-97 DOI: 10.1017/jfm.2012.132.

11. E. Lauer, X. Y. Hu, S. Hickel, and N. A. Adams, Numerical modelling and investigation of symmetric and asymmetric cavitation bubble dynamics, *Computers & Fluids* **69**, (2012), p. 1-19 DOI: 10.1016/j.compfluid.2012.07.020.

12. P. B. Robinson, J. R. Blake, T. Kodama, A. Shima, and Y. Tomita, Interaction of cavitation bubbles with a free surface, *Journal of Applied Physics* **89**, 12 (2001), p. 8225-8237 DOI: 10.1063/1.1368163.

13. O. Supponen, P. Kobel, and M. Farhat, The inner world of a collapsing bubble, *Physics of Fluids* **27**, 091113 (2015), DOI: 10.1063/1.4931098.

14. O. Supponen, D. Obreschkow, and P. Kobel, Detailed Jet Dynamics in a Collapsing Bubble, *Journal of Physics: Conference Series 656 (2015) 012038* (2015), DOI: 10.1088/1742-6596/656/1/012038.

15. D. Obreschkow, M. Tinguely, N. Dorsaz, P. Kobel, A. de Bosset, and M. Farhat, The Quest for the Most Spherical Bubble, *Experiments in Fluids* **54**, 4 (2013), DOI: 10.1007/s00348-013-1503-9.

16. J. F. Thompson, B. K. Soni, and N. P. Weatherill, Handbook of Grid Generation, (1998), CRC Press

17. K. Ando, A.-Q. Liu, and C.-D. Ohl, Homogeneous Nucleation in Water in Microfluidic Channels, *Physical Review Letters* **109**, 4 (2012), p. 044501.

18. W. Malalasekera and H. Versteeg, An Introduction to Computational Fluid Dynamics: The Finite Volume Method 2nd ed, (2007), Prentice Hall.

19. F. Moukalled, L. Mangani, and M. Darwish, The Finite Volume Method in Computational Fluid Dynamics: An introduction with OpenFOAM and Matlab, Fluid Mechanics and Its Applications, Vol, 113, (2015), Springer International Publishing.

20. L. D. Landau and E. M. Lifshitz, Fluid Mechanics, 2nd ed, Course of theoretical physics, Vol, 6, (1987), Pergamon Press.

21. A. Chorin and J. Marsden, A Mathematical Introduction to Fluid Mechanics, 3rd ed, Texts in Applied Mathematics, (2000), Springer.

22. G. K. Batchelor, An Introduction to Fluid Dynamics Cambridge Mathematical Library, (2000), Cambridge University Press.

23. P. Morse and U. Ingard, Theoretical Acoustics, (1987), Princeton University Press.

24. M. J. Holmes, N. G. Parker, and M. J. W. Povey, Temperature dependence of bulk viscosity in water using acoustic spectroscopy, *Journal of Physics: Conference Series, Anglo-French Physical Acoustics Conference* **269 012011**, (2010), DOI: 10.1088/1742-6596/269/1/012011.

25. J. U. Brackbill, D. B. Kothe, and C. Zemach, A continuum method for modeling surface tension, *Journal of Computational Physics* **100**, (1992), p. 335-354.

26. A. Prosperetti and G. Tryggvason, Computational Methods for Multiphase Flow, (2009), Cambridge University Press.

27. M. J. Ivings, D. M. Causon, and E. F. Toro, On Riemann solvers for compressible liquids, *International Numerical Methods for Fluids* **28**, (1998), p. 395-418 DOI: 10.1002/(SICI)1097-0363(19980915)28:3<395::AID-FLD718>3.0.CO;2-S.

28. W. Wagner and H.-J. Kretzschmar, International Steam Tables - Properties of Water and Steam based on the Industrial Formulation IAPWS-IF97, 2nd ed, (2008), Springer-Verlag Berlin Heidelberg.

29. A. Osterman, M. Dular, and B. Sirok, Numerical simulation of a near-wall bubble collapse in an ultrasonic-field, *Journal of Fluid Science and Technology* **4**, 1 (2009), p. 210-221 DOI: 10.1299/jfst.4.210.

30. E. Toro, Riemann Solvers and Numerical Methods for Fluid Dynamics: A Practical Introduction, (2009), Springer-Verlag Berlin Heidelberg.

31. I. Demirdžić, Ž. Lilek, and M. Perić, A collocated finite volume method for predicting flows at all speeds, *International Journal for Numerical Methods in Fluids* **16**, 12 (1993), p. 1029-1050 DOI: 10.1002/fld.1650161202.

32. ANSYS Inc. Fluent 16.1 manual, (2015).

33. O. Ubbink. Numerical prediction of two fluid systems with sharp interfaces, (1997), Imperial College London.

34. V. Gopala and B. van Wachem, Volume of fluid methods for immiscible-fluid and free-surface flows, *Chemical Engineering Journal* **141**, (2008), p. 204-221 DOI: 10.1016/j.cej.2007.12.035.

35. O. Supponen, P. Kobel, and M. Farhat, V0084: The inner world of a collapsing bubble. in *67th Annual Meeting of the APS Division of Fluid Dynamics (November 23, 2014 — November 25, 2014) - See more at: http://gfm.aps.org/meetings/dfd-2014/5417591d69702d585c660300#sthash.D6jo3NUE.dpuf*, 2014.

36. M. R. Ansari and A. Daramizadeh, Numerical simulation of compressible two-phase flow using a diffuse interface method, *International Journal of Heat and Fluid Flow* **42**, (2013), p. 209-223 DOI: 10.1016/j.ijheatfluidflow.2013.02.003.

37. G. Wang, S. Zhang, M. Yu, H. Li, and Y. Kong, Investigation of the shock wave propagation characteristics and cavitation effects of underwater explosion near boundaries, *Applied Ocean Research* **229**, 19 (2014), p. 40-53 DOI: 10.1016/j.apor.2014.02.003.

38. A. Daramizadeh and M. R. Ansari, Numerical simulation of underwater explosion near air-water free surface using a five-equation reduced model, *Ocean Engineering* **110**, Part A (2015), p. 25-35 DOI: 10.1016/j.oceaneng.2015.10.003.

39. P. G. Drazin and W. H. Reid, Hydrodynamic stability, 2nd ed, Cambridge Mathematical Library, (2004), Cambridge University Press.

610   40.   G. S. Settles, Schlieren and Shadowgraph Techniques: Visualizing Phenomena in Transparent
611   Media, (2001), Springer-Verlag Berlin Heidelberg. 376.
612   41.   K. Kolanski, Surface science: foundations of catalysis and nanoscience, 3rd ed, (2012),
613   Wiley. 574.
614   42.   D. Fuster, G. Hauke, and C. Dopazo, Influence of the accommodation coefficient on
615   nonlinear bubble oscillations, *Journal of Acoustical Society of America* **128**, 1 (2010), p. 5-
616   10 DOI: 10.1121/1.3436520.
617   43.   E. W. Lemmon, M. L. Huber, and M. O. McLinden. NIST Standard Reference Database 23:
618   Reference Fluid Thermodynamic and Transport Properties-REFPROP, Version 9.1, (2013),
619   National Institute of Standards and Technology, Standard Reference Data Program,
620   Gaithersburg.
621   44.   O. Baghdassarian, H.-C. Chu, B. Tabbert, and G. A. Williams, Spectrum of Luminescence
622   from Laser-Created Bubbles in Water, *Physical review letters* **86**, 21 (2001), p. 4934-4937
623   DOI: 10.1103/PhysRevLett.86.4934.

624

625